Research Article Vol. 31, No. 2 / 16 Jan 2023 / Optics Express 792
Optics EXPRESS

Harmonic generation from silicon membranes at visible and ultraviolet wavelengths

K. A. Hallman,[1] L. Rodríguez-Suné,[2,*] J. Trull,[2] C. Cojocaru,[2] M. A. Vincenti,[3] N. Akozbek,[4] R. Vilaseca,[2] and M. Scalora[5]

[1]PeopleTec, Inc. 4901-I Corporate Dr. Huntsville, AL 35805, USA
[2]Department of Physics, Universitat Politècnica de Catalunya, 08222 Terrassa, Spain
[3]Department of Information Engineering – University of Brescia, Via Branze 38, 25123 Brescia, Italy
[4]US Army Space & Missile Defense Command, Tech Center, Redstone Arsenal, AL 35898, USA
[5]DEVCOM Aviation and Missile Center, Redstone Arsenal, AL 35898-5000, USA
*laura.rodriguez.sune@upc.edu

Abstract: Nonlinear silicon photonics offers unique abilities to generate, manipulate and detect optical signals in nano-devices, with applications based on field localization and large third order nonlinearity. However, at the nanoscale, inefficient nonlinear processes, absorption, and the lack of realistic models limit the nano-engineering of silicon. Here we report measurements of second and third harmonic generation from undoped silicon membranes. Using experimental results and simulations we identify the effective mass of valence electrons, which determines second harmonic generation efficiency, and oscillator parameters that control third order processes. We can then accurately predict the nonlinear optical properties of complex structures, without introducing and artificially separating the effective $\chi^{(2)}$ into surface and volume contributions, and by simultaneously including effects of linear and nonlinear dispersions. Our results suggest that judicious exploitation of the nonlinear dispersion of ordinary semiconductors can provide reasonable nonlinear efficiencies and transformational device physics well into the UV range.

1. Introduction

Recent years have witnessed impressive progress in the development of functional, nonlinear silicon photonic devices whose manufacture has been enabled by progress in nano-fabrication techniques [1]. These devices can emit light, modulate signals electro-optically and process data at speeds higher than electronic chips, and they are highly compatible with CMOS technology at low cost [2,3]. Applications include frequency conversion [4], optical switches and modulators [5], high-speed optical signal processing [6–8], optical sensing [9], integrated quantum photonic circuits [10]. Understanding how light interacts at the nanometer scale with semiconductors, silicon in particular, is crucial in any device engineering effort, especially in new, highly-dispersive/absorptive wavelength ranges, where light-matter interactions can display new physical phenomena that may not be explained by conventional approaches and approximations.

Harmonic generation is one of the most fundamental processes in nonlinear optics. Traditionally, second and third harmonic generation (SHG and THG) have been studied in transparent materials and under phase matching conditions, mostly in search of large conversion efficiencies. Under the most common scenarios, the dominant nonlinear polarization term is the bulk electric dipole contribution, as exemplified by the nonlinear susceptibilities $\chi^{(2)}$ and $\chi^{(3)}$. However, at the nanoscale bulk interactions are minimized and scenarios altered: surface, quadrupole-like and magnetic nonlinear sources can dominate second order interactions, while third order effects may be triggered or assisted by cascading or higher order nonlinearities.

Silicon is an example of a centrosymmetric material, where the bulk electric dipole contribution is absent. SHG in media with inversion symmetry has been studied since the early days of

#472036 https://doi.org/10.1364/OE.472036
Journal © 2023 Received 15 Aug 2022; revised 10 Oct 2022; accepted 12 Oct 2022; published 3 Jan 2023

Optics EXPRESS

nonlinear optics. One of the first detailed theoretical discussions of surface SHG emanating from quadrupole-like and magnetic dipole terms is found in [11]. In [12], reflected SHG was discussed in the context of a thin slab of crystalline silicon. In [13], a study of SHG was performed on crystalline silicon samples having different crystallographic orientations. Additional studies of THG were carried out in the years that ensued [14–16]. More recently, researchers have taken measures to overcome the absence of a $\chi^{(2)}$ term by depositing either straining layers on top of the silicon [17,18], or by using another $\chi^{(2)}$ nonlinear electro-optic active material as a cladding [19]. Studies on THG from silicon samples having different geometries have also been carried out with the aim to enhance the harmonic signal [20–23].

Most current theoretical models of SHG rely on the description of the bulk parameters and on the introduction of phenomenological or effective surface parameters, as shown in Refs. [24,25]. However, while harmonic generation triggered by surface and magnetic nonlinearities is always present in all materials, they are preemptively neglected in most theoretical descriptions of metasurfaces and other nanometric structures in favor of bulk, dipolar $\chi^{(2)}$ without properly assessing their relevance. In addition, typical approaches focus on an instantaneous medium response that lacks a detailed dynamical description of light-matter interactions, that ultimately neglect aspects relating to the microscopic origin of the generated signals, temporal dynamics, the presence of nonlinear dispersion and competing nonlinearities, possible contributions beyond the third order nonlinearity, pump depletion, and frequency down-conversion. At the nanoscale, these phenomena compete and can even overcome the bulk contribution, and thus require special attention.

In what follows we present experimental measurements of the spectral response and angular dependence of transmitted SHG and THG from crystalline silicon membranes in the visible and UV ranges. Measurements are compared with numerical results predicted by our theoretical hydrodynamic-Maxwell model, which accounts for the aforementioned phenomena and uses as starting point the approach outlined in Refs. [26–28], implements the diverse possible contributions to the nonlinear polarization, and yields unprecedented agreement with experimental observations. The method allows us to identify, distinguish and explain the different nonlinear contributions to the harmonics generated by silicon at the nanoscale at visible and UV wavelengths. We measure and estimate the efficiency of the nonlinear signal making no assumptions about effective surface or volume nonlinearities. The only free parameters present in the model are (1): the effective mass of bound electrons, which determines SHG triggered by symmetry breaking at the surface (i.e. spatial derivatives of the electric field,) and by the magnetic Lorentz force, which can act as a catalyst; and (2) the strength of the cubic nonlinearity, which accounts for nonlinear material dispersion, i.e. $\chi^{(3)}_{\omega}(\omega)$ and $\chi^{(3)}_{3\omega}(\omega)$.

2. Experimental setup

The setup used to measure SH and TH signals in transmission is shown in Fig. 1(a). An amplified Ti:Sapphire laser system (Coherent Astrella) pumping an optical parametric amplifier (OPA) (Coherent Opera Solo) is used as a source of tunable femtosecond pulses. Residual SH and TH beams are filtered out of the OPA beam using both dielectric and color glass filters placed before the sample. Neutral density filters and a pair of crossed polarizers adjusted the pump power, while a third polarizer in the detection arm selected the harmonic signal polarization. A pair of calcium fluoride lenses focused the pump and collected the harmonic beams. A mirror on a flip mount allowed the selection of either a calibrated silicon photodiode, or a more sensitive photomultiplier tube (PMT), to enable easy measurements of the responsivity of the system. This calibration allows calculation of the efficiency of the energy transferred into the harmonic beams using the responsivity and transmission or reflection of the optics. The electronic signal from the PMT was filtered and amplified by a low-noise preamplifier before being measured with a digital

Optics EXPRESS

oscilloscope connected to a computer. Our setup can accurately detect harmonic conversion efficiencies as low as 10^{-13}.

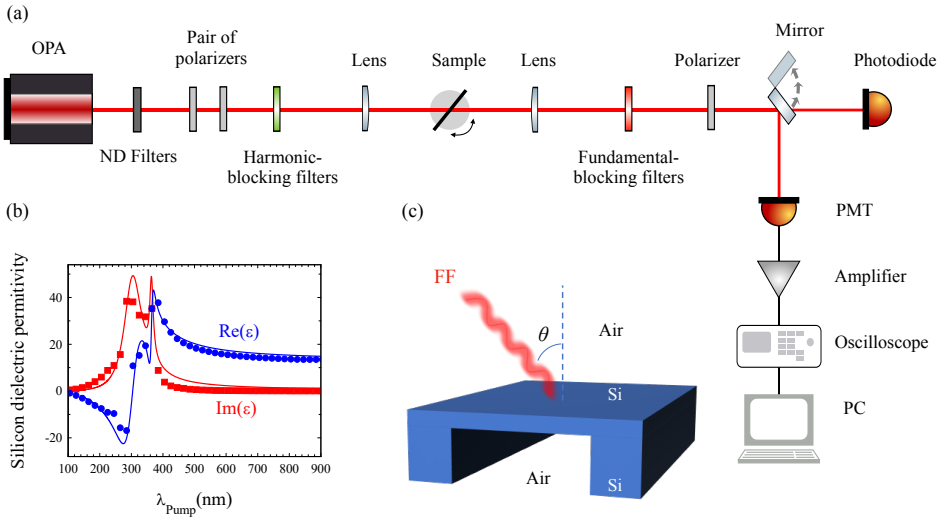

Fig. 1. (a) Experimental setup developed to measure second and third harmonic signals from the silicon membranes as a function of angle of incidence, polarization and pump wavelength. By carefully choosing the filters before and after the sample, we are able to filter harmonic signals coming from previous elements of the setup and attenuate the pump radiation such that the only signal detected at the PMT/Photodiode is either SH or TH generated by the sample. (b) Real (blue circle markers) and imaginary (red square markers) parts of the complex dielectric constant of silicon found in Palik's handbook [32]. The respective solid curves are the corresponding Lorentzian functions chosen to reproduce the data. (c) The sample is a single-crystal undoped <100> silicon membrane suspended over a frame.

The samples were mounted on a custom goniometer with six degrees of freedom, and the angle of incidence could be adjusted using a motorized rotation stage connected to the same computer. For each point in the pump wavelength sweeps, the pump wavelength was changed manually, the laser energy adjusted to compensate for the wavelength-dependent OPA efficiency, and a separate responsivity value was used. Although measurements like these typically use a prism and slit to reduce the number of filters needed to remove the pump beam [29–31], alignment with a multi-wavelength system and pump-wavelength sweeps would be difficult with this configuration. Instead, several filters were used to remove the unwanted beams, and the filter choice was crucial. Dielectric filters were often found to generate their own harmonic signature, so they were always used in conjunction with colored glass filters, and the total optical density for all filters must exceed the harmonic generation efficiency to ensure there is no pump leakage through the filters. For the SH measurements, band pass filters and colored glass filters removed the pump beam, TH beam, and any other optical noise. If the TH wavelength was tuned in the visible region, only color glass filters were used to enable sweeping the pump wavelength in finer steps than would be possible with band pass filters. However, the TH results were confirmed with band pass filters when the harmonic wavelength allowed. For third harmonics found in the UV region, band pass filters were used, and the wavelength was not swept because of a decreased sensitivity of the PMT. The membranes, sketched in Fig. 1(c), were purchased from Norcada (Alberta, Canada) and consist of 200nm- and 1340nm-thick <100> silicon membranes etched out of silicon wafers. The linear dielectric constant of undoped crystalline silicon (Fig. 1(b)) displays

Optics EXPRESS

two prominent resonances in the UV range that are fitted using two separate Lorentzian functions (also shown in Fig. 1(b)), appropriately detuned, and having different plasma frequencies and damping coefficients.

In Fig. 2(a) we display linear pump transmittance vs. incident carrier wavelength for 200nm- and 1340nm-thick membranes. The spectra consists of a series of Fabry-Perot resonances whose free spectral range depends on thickness. In Fig. 2(b) we show the transmittance around the 1400nm resonance peak, when low-intensity, 100fs pulses are injected normal to the surface of the 1340nm-thick membrane. Simulations and measurements of the linear transmittance agree well in terms of amplitude and peak location.

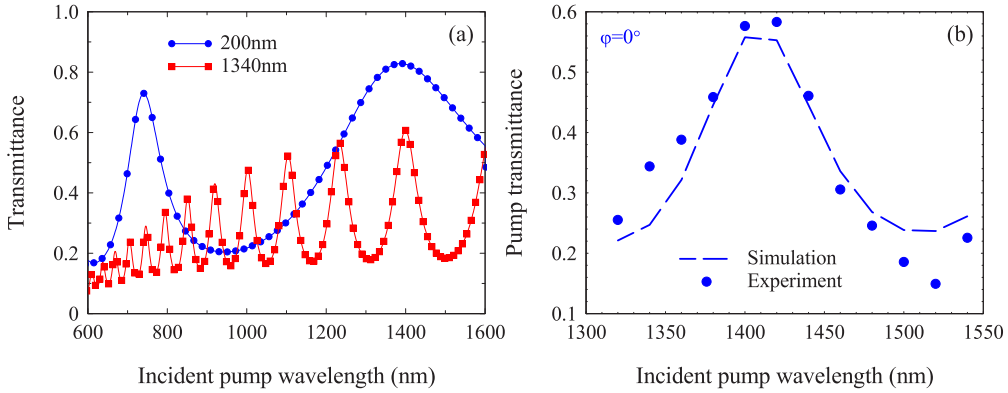

Fig. 2. (a) Transmittance vs incident pump wavelength for the 200nm- and 1340nm–thick Si membranes. Both samples display Fabry-Perot resonances according to their thicknesses. (b) Pump transmittance vs. carrier wavelength for normally incident 100fs pulses tuned near the 1400nm resonance wavelength for the 1340nm–thick membrane. The dashed curve represents data extracted from the simulations, while the solid markers denote measurements.

3. Results

In this section we show our experimental results regarding the nonlinear behavior of the two silicon membranes, and compare them with the predictions of our simulations. The theoretical approach that we pursue thus includes two separate bound electron species, as shown in Fig. 1(b). We do not consider contributions from conduction electrons or holes because we assume the medium is undoped (doping densities $< 10^{14}\text{cm}^{-3}$) and pumping occurs at wavelengths that correspond to energies below what is required to excite valence electrons into the conduction band. We first recorded transmitted SHG and THG efficiencies as functions of incident carrier wavelength and angle for the 1340nm-thick membrane. TM-polarized SH and TH signals were detected for input TM polarization for incident peak power densities that ranged from 1.5GW/cm^2 to 15GW/cm^2. THG data are shown in Fig. 3(a), where we report the spectral response for normal and oblique angles of incidence. A maximum THG efficiency of 2×10^{-9} is obtained at 466nm, with the pump tuned to 1400nm at normal incidence. Simulations and measurements agree well in terms of amplitude and peak location. The agreement between theory and experimental observations evident in Fig. 3(a) repeats in Fig. 3(b), where we show the angular response of the TH signal when tuned to the peak of transmission located near 1400nm. Other spectral locations that were tested yielded similar degree of agreement between simulation and measurement.

The predicted and observed angular dependence and conversion efficiencies of the generated SH signal are depicted in Figs. 4(a)-(c) for three different carrier wavelengths. An incident pulse having peak power density of approximately 15GW/cm^2 generates SH signals with maxima

Optics EXPRESS

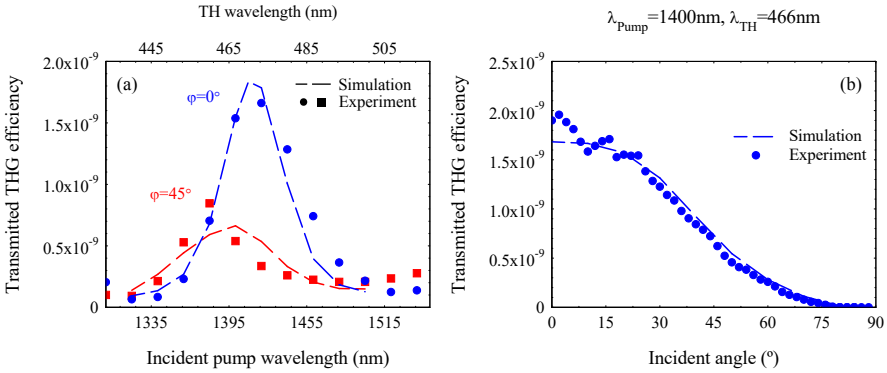

Fig. 3. (a) Measured and simulated THG spectra for the 1340nm-thick membrane. Markers exemplify the data obtained at 0° (filled blue circles) and 45° (filled red squares); corresponding simulations for 0° (dashed blue curve) and 45° (dashed red curve). (b) Transmitted THG conversion efficiency vs incident angle for the 1340nm-thick membrane. The carrier wavelength of incident pulses is tuned near the peak of transmission located at 1400 nm.

peaking between 65° and 70°, and conversion efficiencies of order 10^{-12}. This response is more than two orders of magnitude weaker compared to the response observed in a noble metal like gold [30]. Using our model, we estimate it to be about the same as that of an isotropic, centrosymmetric glass like fused silica. According to the hydrodynamic-Maxwell approach outlined in Refs. [26–29] and in the appendix, SHG conversion efficiencies are completely determined by the spatial derivatives of the electric field, and by the magnetic component of the Lorentz force, which is intrinsically nonlinear but is almost never explicitly and specifically discussed. Each of these terms multiplies identical coefficients that are inversely proportional to a single unknown parameter, i.e., the effective mass of bound electrons. Therefore, it is reasonable to conclude that by matching the simulated and measured conversion efficiencies, the model should allow us to estimate the effective mass of valence electrons. We note that these electrons are almost never discussed in the context of the physics of semiconductors, which emphasize the excitation of valence electrons into the conduction band and the holes that they leave behind. If these dynamics were to occur by appropriately doping the material, it would significantly change the dielectric response depicted in Fig. 1. Accordingly, one could then modify the model by introducing Drude-like contributions from both free (negative) electrons and (positive) holes, each with their respective physical properties, and expect the manifestation of new phenomena.

The presence of the magnetic component of the Lorentz force is essential when the pump is TE-polarized, and can act like a powerful catalyst when the field is TM-polarized. In fact, in centrosymmetric systems having two-dimensional symmetry, like those we have studied, a TE-polarized pump generates a TM-polarized SH signal. The pivotal terms that make this possible are found only in the magnetic component of the Lorentz force, i.e., $\frac{e\lambda_0}{m^*_{bj}c^2}\dot{\mathbf{P}}_{bj}\times\mathbf{H}$. For TM-polarized pumps, calculations clearly show that while the individual surface component may yield several orders of magnitude more SH signal than the magnetic Lorentz term, their combined effect can impact both quantitative and qualitative aspects of the interaction. This situation is depicted in Fig. 4(d). SHG triggered *only* by the magnetic term is two orders of magnitude smaller than the SH signals generated *only* by the surface term, and barely visible on the plot. Nevertheless, when both terms are present (solid curves) the peak transmitted SH signal suffers a near-20% reduction compared to what is generated by the surface, while the reflected SH peak

Optics EXPRESS

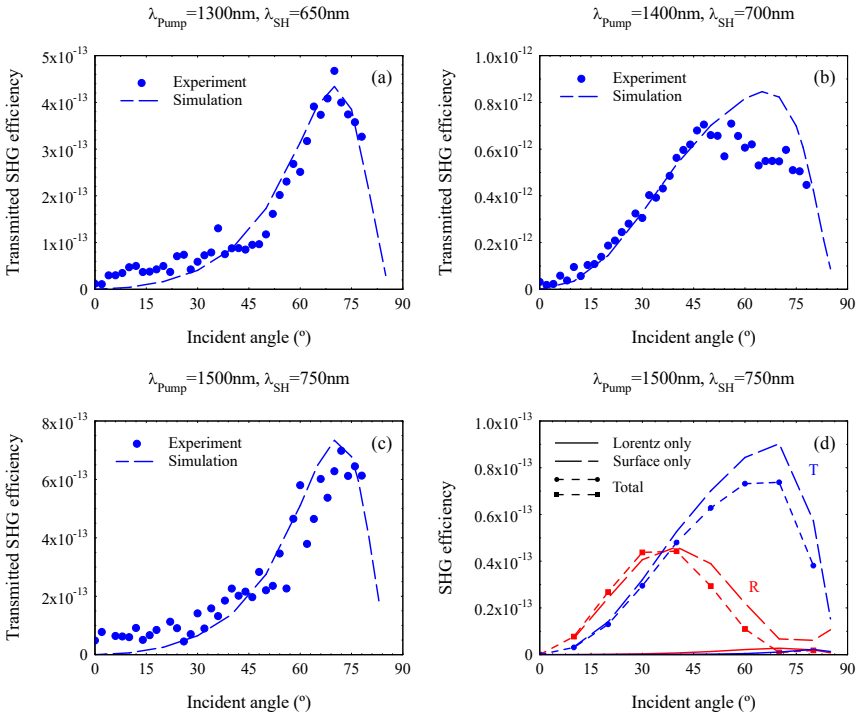

Fig. 4. Angular dependence of transmitted SHG for incident pulses tuned to: (a) 1300 nm, (b) 1400 nm, and (c) 1500 nm. The shapes of each of the curves is sensitive to tuning. The responses are classic examples of SHG from a centrosymmetric medium. (d) SHG calculated by selectively suppressing either the surface or the magnetic Lorentz terms, using 100fs pulses having peak power density 1.5 GW/cm^2. SHG triggered by the magnetic term (solid curves), by the surface term (dashed curves), and when both terms are present (solid markers). The total transmitted SH signal decreases by nearly 20% compared to what only the surface yields, while the reflected SH peak shifts by approximately 5° when both terms are included.

shifts to smaller angles by a measurable amount. Hence the attribution of catalytic action on the magnetic Lorentz term. The dynamical implications of these results cannot be overstated, and strongly caution against the mere separation of effective "surface" and "volume" nonlinearities, or the neglect of the magnetic Lorentz force because by itself it would seem to yield a SH signal that may appear to be too small to matter. Comparison of measurements and simulations suggest $m_0{}^* \sim 2.5m_e$, where m_e is the free electron mass. Of course, these circumstances are unique to silicon and the geometry under consideration, may change accordingly, and should be assessed in a case-by-case basis.

The second set of measurements consisted of detecting THG efficiencies carried out on a ~200nm-thick silicon membrane. This sample gives us the opportunity to directly address the nanoscale, and to simultaneously investigate THG in a cavity environment in the UV range, where nonlinear dispersion, absorption, and phase-locking come robustly into play [28,31,33]. In Fig. 5(a) we show the linear transmission spectrum at normal incidence for this sample (right y-axis), along with both measured and simulated transmitted THG spectra for normal and oblique angles of incidence. In Figs. 5(b)–(d) we display the angular dependence of the TH signal on the

Optics EXPRESS

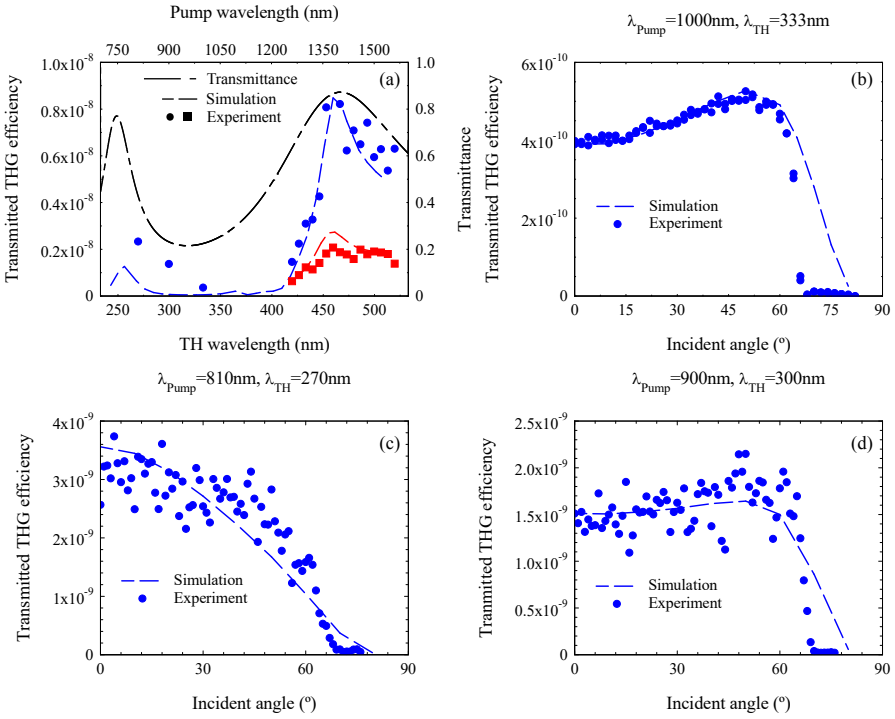

Fig. 5. (a) Measured and simulated THG spectra for a suspended, 200nm-thick silicon membrane. The markers exemplify the data obtained at 0° (filled blue circles) and 45° (filled red squares); corresponding simulations for 0° (dashed blue curve) and 45° (dashed red curve). The dashed black curve is the measured transmittance from the sample at normal incidence. (b) Measured and simulated angular response of the TH signal for 100fs pulses tuned to 1000 nm, where a minimum of THG is predicted. (c) and (d) Same as (b), with the pump tuned to 810 nm and 900 nm, respectively. The beam spills outside the membrane and into the substrate if the incident angle is larger than approximately 70°, drastically reducing overall transmittance from the sample. The simulations are performed without the substrate.

angle of incidence when the pulse carrier wavelength is tuned to 1000nm (b), at the bottom of the transmission curve, as well as 810nm (c), and 900nm (d). The sharp drops that the observed TH signal display in Figs. 5(b)–(d) occurs because the incident beam impinges on the substrate, with subsequent precipitous reduction in transmittance. The aperture of the 200nm-thick membrane is smaller compared to that of the 1340nm-thick sample, thus restricting the range of incident angles we can investigate without having the laser beam clipped by the membrane aperture. For simplicity, the simulations do not take the substrate into account. Worthy of note is the fact that the 200nm-thick membrane is at least five times more efficient than the thicker counterpart in Fig. 3(a), and that conversion efficiencies are still relatively large even when the TH signal is tuned to 270nm. Predicted and observed data display remarkable agreement in the wavelength range above 300nm, which is unprecedented based on the results available in the literature, a fact that gives us enough confidence about our understanding of the processes that play a role on and off-resonance, as well as our theoretical approach. However, we remark that in Fig. 5(a), on-axis THG predictions below 300nm have the right trend but are somewhat lower than our experimental observations. This is likely partially due to the imperfect Lorentzian fit depicted in

Optics EXPRESS

Fig. 1(b), where a shallow, rudimentary shoulder of a third resonance is barely discernable. This, combined with the fact that conversion efficiency is inversely proportional to the fourth power of the number density and lattice constant (see Appendix), and the possibility that the third order coefficient may also be somewhat dispersive and geometry dependent, can account for stronger nonlinear gain. As a result, Figs. 5(c) and 5(d) were obtained by slightly increasing the nonlinear gain coefficient to approximately match observed conversion efficiencies. This action leaves the shape of the curves unaffected.

4. Conclusion

In summary, we have studied nonlinear frequency conversion in suspended silicon membranes of 200nm- and 1340nm-thick, in the visible and UV ranges, in regimes where silicon tends to be opaque, and where nonlinear dispersion and phase-locking dominate the dynamics. Our theoretical approach, based on the hydrodynamic-Maxwell model, is in remarkable agreement with measured results, and sheds light on the dynamical aspects of surface, second order phenomena, as well as third order nonlinearities. The identification of basic parameters like the effective mass of bound electrons, which drives SHG, and nonlinear oscillator parameters, which control THG, will allow us to make accurate predictions about conversion efficiencies in more complicated geometrical arrangements. Our results thus suggest that the entire UV range is available for the development of relatively efficient light sources.

5. Appendix

We consider two bound electron species having different effective plasma frequencies and damping. While we refer the reader to Refs. [26–29] for details, here we limit ourselves to reproducing the basic material equations of motion and to briefly discuss their content:

$$\ddot{\mathbf{P}}_{bj} + \tilde{\gamma}_{bj}\dot{\mathbf{P}}_{bj} + \tilde{\omega}_{0,bj}^2\mathbf{P}_{bj} - \tilde{\beta}_j(\mathbf{P}_{bj}\bullet\mathbf{P}_{bj})\mathbf{P}_{bj} = \frac{n_{0,bj}e^2\lambda_0^2}{m_{bj}^*c^2}\mathbf{E} + \frac{e\lambda_0}{m_{bj}^*c^2}(\mathbf{P}_{bj}\bullet\nabla)\mathbf{E} + \frac{e\lambda_0}{m_{bj}^*c^2}\dot{\mathbf{P}}_{bj}\times\mathbf{H} \quad (1)$$

$\mathbf{P}_{bj}$ is the bound polarization, $j = 1{,}2$ represent two separate atomic species. The total polarization inserted into Maxwell's equation is the vector sum $\mathbf{P}_{Total} = \mathbf{P}_{b1} + \mathbf{P}_{b2}$. Spatial and temporal derivatives are performed with respect to the following scaled coordinates:$\tau = ct/\lambda_0;\ \tilde{x},\ \tilde{y},\ \tilde{z} = x/\lambda_0,\ y/\lambda_0,\ z/\lambda_0$, where $\lambda_0 = 1\mu$m is a convenient reference wavelength, and c is the speed of light in vacuum. Equation (1) does not include a second order bulk nonlinearity because silicon is centrosymmetric, although its inclusion is straightforward for non-centrosymmetric materials [31]. If we consider only the linear terms and take the Fourier transform of Eq. (1), we recover the local, linear dielectric response, which may be written as: $\varepsilon(\tilde{\omega}) = 1 - \frac{\tilde{\omega}_{p1}^2}{(\tilde{\omega}^2-\tilde{\omega}_{01}^2+i\tilde{\gamma}_{b1}\tilde{\omega})} - \frac{\tilde{\omega}_{p2}^2}{(\tilde{\omega}^2-\tilde{\omega}_{02}^2+i\tilde{\gamma}_{b2}\tilde{\omega})}$, with $(\tilde{\omega}_{p1},\ \tilde{\omega}_{01},\ \tilde{\gamma}_{b1}) = (3,\ 2.75,\ 0.1)$ and $(\tilde{\omega}_{p2}, \tilde{\omega}_{02}, \tilde{\gamma}_{b2}) = (11,\ 3.3,\ 0.75)$. The magnitude of the dielectric constant is never explicitly stated, but may be determined via Eqs. (1) if so desired [29]. The parameter $\tilde{\beta}_j \approx \omega_{0,bj}^2\lambda_0^2/(L^2n_{0bj}^2e^2c^2)$ may be derived from the nonlinear oscillator model under consideration. THG conversion efficiency is proportional to $\tilde{\beta}_j^2 \sim (L^4n_{0bj}^4)^{-1}$. While for our purposes it may suffice to assume that $\tilde{\beta}_j$ is constant, and that $\tilde{\beta}_1 \approx \tilde{\beta}_2$ since the resonances are closely spaced, in reality the two electron species probably have different densities and electron masses, n_{0bj} and m_{bj}, respectively. From a classical point of view, L represents the taut length of a spring, but it also embodies the approximate lattice constant, or the diameter of the participating orbital [34]. Combining these parameters, we obtain $\tilde{\beta}_j \approx 1.5\times10^{-8}$, which leads to $\chi_\omega^{(3)} \approx 10^{-18}$ and $\chi_{3\omega}^{(3)} \approx 10^{-18}$. We remark that the magnitude of $\tilde{\beta}_j$ is inversely proportional to the square of both particle density and lattice constant, and may also be dispersive and depend on shape factors dictated by the geometry. In addition, an improved Lorentzian fit of the dielectric

Optics EXPRESS

constant with an additional resonance below 300nm can affect its magnitude. As a result, a more realistic view is that the magnitude of $\tilde{\beta}_j$ is in fact somewhat flexible.

Surface $\frac{e\lambda_0}{m^*_{bj}c^2}(\mathbf{P}_{bj} \bullet \nabla)\mathbf{E}$ and magnetic Lorentz $\frac{e\lambda_0}{m^*_{bj}c^2}\dot{\mathbf{P}}_{bj} \times \mathbf{H}$ contributions, as well as the bulk nonlinearity $\tilde{\beta}_j(\mathbf{P}_{bj} \bullet \mathbf{P}_{bj})\mathbf{P}_{bj}$, are fully expanded in their fundamental and harmonic components, yielding dozens of terms that fully account for pump depletion and up- and down-conversion contributions. We point out that the high local field intensities that develop in Mie resonances of the type discussed in Ref. [28] may require the addition of higher order nonlinear contributions. For instance, for the nanowire metasurface in question the local electric and magnetic field intensities may be amplified in excess of two and three orders of magnitude, respectively. As a result, instead of the term $\tilde{\beta}_j(\mathbf{P}_{bj} \bullet \mathbf{P}_{bj})\mathbf{P}_{bj}$ one may adopt an expansion of the nonlinearity that includes additional orders, for instance, $\tilde{\beta}_j(\mathbf{P} \bullet \mathbf{P})\mathbf{P} - \tilde{\Theta}_j(\mathbf{P} \bullet \mathbf{P})^2\mathbf{P} + \tilde{\Delta}_j(\mathbf{P} \bullet \mathbf{P})^3\mathbf{P}$. It is straightforward to show that $\tilde{\Theta}_j = \frac{\tilde{\beta}_j}{n^2e^2L^2}$, $\tilde{\Delta}_j = \frac{\tilde{\beta}_j}{n^4e^4L^4}$, and that each of these terms contributes to the total $\chi^{(3)}$ response. Our parameter choice yields $\tilde{\Theta}_j \approx 10^{-17}$ and $\tilde{\Delta}_j \approx 10^{-25}$. Examples of just a few of the many non-instantaneous terms contributing to the full $\chi^{(3)}_\omega$ response are proportional to $\tilde{\beta}_j|P_\omega|^2P_\omega$, $\tilde{\Theta}_j|P_\omega|^4P_\omega$, and $\tilde{\Delta}_j|P_\omega|^6P_\omega$. Similarly, some of the terms contributing to $\chi^{(3)}_{3\omega}$ are proportional to $\tilde{\beta}_j{P_\omega}^3$, $\tilde{\Theta}_j|P_\omega|^2{P_\omega}^3$, $\tilde{\Delta}_j|P_\omega|^4{P_\omega}^3$. The difference then becomes evident, between the approach exemplified by Eq. (1), and any other method that makes the assumption that the entire third order response may be summarized by instantaneous terms like $\chi^{(3)}|E_\omega|^2E_\omega$ and $\chi^{(3)}_{3\omega}{E_\omega}^3$, which do not account for dynamical consequences of explicitly introducing higher order nonlinearities, and specifically elude proper accounting of nonlinear dispersion.

Funding. Agencia Estatal de Investigación (PID2019-105089GB-I00/AEI/10.13039750110001 1033); Research, Development and Engineering Command (W911NF1920279).

Acknowledgments. The authors thank Zack Coppens and Dana Dement for useful discussions and help with the sample. LRS, JT, and CC acknowledge to US Army Research Laboratory Cooperative Agreement N° W911NF1920279 issued by US ARMY ACC-APG-RTP and Spanish Agencia Estatal de Investigación (project no. PID2019-105089GB-I00/AEI/10.13039750110001 1033). MAV was partially sponsored by the Army Research Laboratory under Cooperative Agreement N° W911NF2020078.

Disclosures. The authors declare no conflicts of interest.

Data availability. Data underlying the results presented in this paper are not publicly available at this time but may be obtained by the authors upon reasonable request.

References

1. J. Leuthold, C. Koos, and W. Freude, "Nonlinear silicon photonics," Nature Photonics **4**, 535–544 (2010). M. Lipson, "Guiding, modulating, and emitting light on silicon-challenges and opportunities," J. Lightwave Technol. 23, 4222–4238 (2005).
2. D. Van Thourhout, J. Van Capenhout, P. Rojo-Romeo, P. Regreny, C. Seassal, P. Binetti, X. J. M. Leijtens, R. Nötzel, M. K. Smit, L. Di Cioccio, C. Lagahe, J. M. Fedeli, and R. Baets, "Photonic interconnect layer on CMOS," *Proc. 33rd European Conf. Optical Communications paper 6.3.1* (2007).
3. L. Tsybeskov, D. J. Lockwood, and M. Ichikawa, "Silicon Photonics: CMOS Going Optical," Proc. IEEE **97**(7), 1161–1165 (2009).
4. M. A. Foster, A. C. Turner, R. Salem, M. Lipson, and A. L. Gaeta, "Broad-band continuous-wave parametric wavelength conversion in silicon nanowaveguides," Opt. Express **15**(20), 12949–12958 (2007).
5. M. Lipson, "Guiding, modulating, and emitting light on silicon-challenges and opportunities," J. Lightwave Technol. **23**(12), 4222–4238 (2005).
6. Y.-H. Kuo, H. Rong, V. Sih, S. Xu, M. Paniccia, and O. Cohen, "Demonstration of wavelength conversion at 40 Gb/s data rate in silicon waveguides," Opt. Express **14**(24), 11721–11726 (2006).
7. M. A. Foster, R. Salem, D. F. Geraghty, A. C. Turner-Foster, M. Lipson, and A. L. Gaeta, "Silicon-chip-based ultrafast optical oscilloscope," Nature **456**(7218), 81–84 (2008).
8. C. Koos, P. Vorreau, T. Vallaitis, P. Dumon, W. Bogaerts, R. Baets, B. Esembeson, I. Biaggio, T. Michinobu, F. Diederich, W. Freude, and J. Leuthold, "All-optical high-speed signal processing with silicon-organic hybrid slot waveguides," Nat. Photonics **3**(4), 216–219 (2009).
9. J. T. Robinson, L. Chen, and M. Lipson, "On-chip gas detection in silicon optical microcavities," Opt. Express **16**(6), 4296–4301 (2008).

Optics EXPRESS

10. A. W. Elshaari, W. Pernice, K. Srinivasan, O. Benson, and V. Zwiller, "Hybrid integrated quantum photonic circuits," Nat. Photonics **14**(5), 285–298 (2020).
11. E. Adler, "Nonlinear Optical Frequency Polarization in a Dielectric," Phys. Rev. **134**(3A), A728–A733 (1964).
12. N. Bloembergen, R. K. Chang, S. S. Jha, and C. H. Lee, "Optical Second-Harmonic Generation in Reflection from Media with Inversion Symmetry," Phys. Rev. **174**(3), 813–822 (1968).
13. H. W. K. Tom, T. F. Heinz, and Y. R. Shen, "Second-Harmonic Reflection from Silicon Surfaces and Its Relation to Structural Symmetry," Phys. Rev. Lett. **51**(21), 1983–1986 (1983).
14. N. Bloembergen, W. K. Burns, and M. Matsuoka, "Reflected third harmonic generated by picosecond laser pulses," Opt. Commun. **1**(4), 195–198 (1969).
15. W. K. Burns and N. Bloembergen, "Third harmonic generation in absorbing media of cubic or isotropic symmetry," Phys. Rev. B **4**(10), 3437–3450 (1971).
16. C. C. Wang, J. Bomback, W. T. Donlon, C. R. Huo, and J. V. James, "Optical Third-Harmonic Generation in Reflection from Crystalline and Amorphous Samples of Silicon," Phys. Rev. Lett. **57**(13), 1647–1650 (1986).
17. M. Cazzanelli, F. Bianco, E. Borga, G. Pucker, M. Ghulinyan, E. Degoli, E. Luppi, V. Véniard, S. Ossicini, D. Modotto, S. Wabnitz, R. Pierobon, and L. Pavesi, "Second-harmonic generation in silicon waveguides strained by silicon nitride," Nat. Mater. **11**(2), 148–154 (2012).
18. J.-H. Zhao, Q.-D. Chen, Z.-G. Chen, G. Jia, W. Su, Y. Jiang, Z.-X. Yan, T. V. Dolgova, O. A. Aktsipetrov, and H.-B. Sun, "Enhancement of second-harmonic generation from silicon stripes under external cylindrical strain," Opt. Lett. **34**(21), 3340–3342 (2009).
19. C. Castellan, A. Trenti, C. Vecchi, A. Marchesini, M. Mancinelli, M. Ghulinyan, G. Pucker, and L. Pavesi, "On the origin of second harmonic generation in silicon waveguides with silicon nitride cladding," Sci. Rep. **9**(1), 1088 (2019).
20. B. Corcoran, C. Monat, C. Grillet, D. J. Moss, B. J. Eggleton, T. P. White, L. O'Faolain, and T. F. Krauss, "Green light emission in silicon through slow-light enhanced third-harmonic generation in photonic-crystal waveguides," Nat. Photonics **3**(4), 206–210 (2009).
21. M. R. Shcherbakov, D. N. Neshev, B. Hopkins, A. S. Shorokhov, I. Staude, E. V. Melik-Gaykazyan, M. Decker, A. A. Ezhov, A. E. Miroshnichenko, I. Brener, A. A. Fedyanin, and Y. S. Kivshar, "Enhanced Third-Harmonic Generation in Silicon Nanoparticles Driven by Magnetic Response," Nano Lett. **14**(11), 6488–6492 (2014).
22. W. Tong, C. Gong, X. Liu, S. Yuan, Q. Huang, J. Xia, and Y. Wang, "Enhanced third harmonic generation in a silicon metasurface using trapped mode," Opt. Express **24**(17), 19661–19670 (2016).
23. S. Sederberg, C. J. Firby, and A. Y. Elezzabi, "Efficient, broadband third-harmonic generation in silicon nanophotonic waveguides spectrally shaped by nonlinear propagation," Opt. Express **27**(4), 4990–5004 (2019).
24. M. Falasconi, L. C. Andreani, A. M. Malvezzi, M. Patrini, V. Mulloni, and L. Pavesi, "Bulk and surface contributions to second-order susceptibility in crystalline and porous silicon by second-harmonic generation," Surf. Sci. **481**(1-3), 105–112 (2001).
25. P. R. Wiecha, A. Arbouet, C. Girard, T. Baron, and V. Paillard, "Origin of second-harmonic generation from individual silicon nanowires," Phys. Rev. B **93**(12), 125421 (2016).
26. M. Scalora, M. A. Vincenti, D. de Ceglia, V. Roppo, M. Centini, N. Akozbek, and M. J. Bloemer, "Second- and third-harmonic generation in metal-based structures," Phys. Rev. A **82**(4), 043828 (2010).
27. M. Scalora, M. A. Vincenti, D. de Ceglia, C. M. Cojocaru, M. Grande, and J. W. Haus, "Nonlinear duffing oscillator model for third harmonic generation," J. Opt. Soc. Am. B **32**(10), 2129–2138 (2015).
28. M. Scalora, J. Trull, C. Cojocaru, M. A. Vincenti, L. Carletti, D. de Ceglia, N. t. Akozbek, and C. De Angelis, "Resonant, broadband, and highly efficient optical frequency conversion in semiconductor nanowire gratings at visible and UV wavelengths," J. Opt. Soc. Am. B **36**(8), 2346–2351 (2019).
29. L. Rodríguez-Suné, J. Trull, N. Akozbek, D. de Ceglia, M. A. Vincenti, M. Scalora, and C. Cojocaru, "Retrieving Linear and Nonlinear Optical Dispersions of Matter: Combined Experiment-Numerical Ellipsometry in Silicon, Gold and Indium Tin Oxide," Front. Photon. 17 Sept. 2021, https://doi.org/10.3389/fphot.2021.746341
30. L. Rodríguez-Suné, J. Trull, C. Cojocaru, N. Akozbek, D. de Ceglia, M. A. Vincenti, and M. Scalora, "Harmonic generation from gold nanolayers: bound and hot electron contributions to nonlinear dispersion," Opt. Express **29**(6), 8581–8591 (2021).
31. L. Rodríguez-Suné, J. Trull, M. Scalora, R. Vilaseca, and C. Cojocaru, "Harmonic generation in the opaque region of GaAs: the role of the surface and magnetic nonlinearities," Opt. Exp. **27**(18), 26120–26130 (2019).
32. E. D. Palik, *Handbook of Optical Constants of Solids* (Academic Press, 1985).
33. J. Gao, M. A. Vincenti, J. Frantz, A. Clabeau, X. Qiao, L. Feng, M. Scalora, and N. M. Litchinitser, "Near-infrared to ultra-violet frequency conversion in chalcogenide metasurfaces," Nat. Commun. **12**(1), 1–5 (2021).
34. https://www.infoplease.com/semimetallics/silicon